Revision 1

Tourmaline composition and boron isotope signature as a tracer of magmatic-hydrothermal processes

Kun-Feng Qiu[1,2,*], Hao-Cheng Yu[1], Callum Hetherington[3], Ya-Qi Huang[1], Tao Yang[2], Jun Deng[1]

1 State Key Laboratory of Geological Processes and Mineral Resources, School of Earth Sciences and Resources, China University of Geosciences, Beijing 100083, China

2 State Key Laboratory for Mineral Deposits Research, Nanjing University, Nanjing 210093, China

3 Department of Geosciences, Texas Tech University, Box 41053, Lubbock, Texas, USA (ORCID ID 0000-0003-1389-8641)

Corresponding author:

Dr. Kun-Feng Qiu

kunfengqiu@qq.com, kunfengqiu@cugb.edu.cn

China University of Geosciences, Beijing

No. 29 Xueyuan Road, Haidian District, Beijing

Tel.: +86-10-82321383

ABSTRACT

This study presents a petrogeochemical and boron isotope study on tourmaline from the barren Damai, and the contemporaneous but ore-bearing Dewulu and Meiwu intrusions, to better understand the origins, sources and fluid evolution of magmatic-hydrothermal ore systems, and provide ore formation implications for gold, copper, and iron deposits in the Xiahe-Hezuo polymetallic district in the West Qinling, China. Tourmaline from all three intrusions shows similar compositions and encompasses Na-Fe schorl and Na-Mg dravite. Tourmaline at Dewulu is primarily found in tuffaceous breccias and quartz diorite porphyry. In the tuffaceous breccia body, tourmaline occurs as fine-grained anhedral masses that fill voids and cement fragments of breccia and sickle quartz. Tourmalines in breccia are texturally similar to those formed in typical breccia pipes, which are attributed to explosion or collapse induced by a transition from magmatic to hydrothermal Si- and B-rich fluids. They display element substitutions controlled by $Fe^{2+}Mg_{-1}$, indicating a reduced environment. Values of $\delta^{11}B$ are −6.6 ‰ to −4.0 ‰, representing the primary magmatic-hydrothermal fluids. Tourmaline from the Dewulu quartz diorite porphyry is coarse-grained, euhedral and found in quartz-sulfide veins. The tourmaline displays oscillatory zoning textures but lack correlative variations of major elements. The $Fe^{2+}Mg_{-1}$ and $Fe^{3+}Al_{-1}$ substitution mechanisms are dominant demonstrating more oxidized fluids. The $\delta^{11}B$ values in the cores, ranging from −7.1 ‰ to −5.6 ‰, suggest that the tourmalines in the quartz veins were inherited from magmatic–hydrothermal

fluids that precipitated the fine-grained tourmaline in the tuffaceous breccia body. A large $\delta^{11}B$ isotopic fractionation that decreases from cores (−5.6 ‰) to rims (−10.7 ‰) indicates a significant fractionation of degassing occurred, increasing oxygen fugacity of the residual liquid. The Meiwu locality hosts fine-grained euhedral tourmalines coexisting with magnetite. Their composition is controlled by substitution between Al^{3+} by Fe^{3+}, and have the lightest $\delta^{11}B$ values ranging from −11.4 to −10.0 ‰. They are interpreted to result from skarn formation under oxidized condition. In contrast, $^{X}\square Al(NaMg)_{-1}$ is the dominant substitution mechanism for Damai tourmalines and attributed to (geochemically) reduced fluids with a low salinity. The assessment concludes that tourmalines with low Fe values, substitution mechanisms dominated by $Fe^{3+}Al_{-1}$, and large shifts of B isotopic composition, have better potentials as an ore-forming indicator in the Xiahe-Hezuo polymetallic district.

Keywords: Tourmaline origin, Textural occurrence, Boron isotope signature, Magmatic-hydrothermal processes, Ore-forming tracer

61 ## INTRODUCTION

62 Magmatic-hydrothermal systems host a wide range of ore deposits in diverse
63 tectonic settings, including porphyry, skarn, and epithermal deposits (Sillitoe
64 2010; Hong et al. 2017; Maner et al. 2019). Tourmaline is a common gangue
65 mineral in many of these deposits worldwide owing to its stability over a wide
66 range of temperature and pressure conditions (Jiang et al. 2008; Marschall and
67 Jiang 2011; Slack and Trumbull 2011). Tourmaline may preserve textural,
68 compositional, and isotopic features during growth and hence reveal considerable
69 detail about the environment in which it crystallized (Mlynarczyk and Williams-
70 Jones 2006; Pal et al. 2010). Consequently, documenting the magmatic and
71 hydrothermal record in tourmaline is an important step for furthering our
72 understanding of the origin and evolution of ore fluids, the mineralizing
73 processes, and thereby providing a potentially valuable tool for mineral
74 exploration (Garda et al. 2009; Hong et al. 2017).

75 The Xiahe-Hezuo polymetallic district located in the Triassic West Qinling
76 Orogen in central China has been the focus of significant (ore deposit)
77 exploration and research in recent years (Jin et al. 2017; Qiu and Deng 2017; Sui
78 et al. 2018; Qiu et al. 2020; Yu et al. 2020a, b). The widespread Triassic
79 magmatism in the district, attributed to northward subduction of the Paleo-Tethys
80 Oceanic slab beneath the South Qinling block, produced dozens of gold, copper
81 and iron deposits (Qiu et al. 2018; Li et al. 2019). Although tourmaline
82 commonly occurs in the felsic granites in quartz-tourmaline veins, and were

83 locally mined as ore, their origins, sources, and relationships with mineralization
84 are incompletely understood.

85 The purpose of this study is to document tourmaline in the barren Damai,
86 and the causative Dewulu and Meiwu intrusions from the Xiahe-Hezuo
87 polymetallic district. The origins and evolution of the tourmaline and the fluids
88 from which they grew are investigated using compositional and isotope analyses.
89 We assess the potential of tourmaline as a fertility indicator in distinguishing
90 mineralized from barren host-granites.

91

92 **GEOLOGICAL BACKGROUND**

93 The roughly WNW-trending West Qinling Orogen extends for 400 km
94 between the North China and South China blocks, occupying a key position in
95 the Central China Orogenic belt (Fig. 1a; Dong and Santosh 2016; Deng et al.
96 2018; Luo et al. 2018). It consists of various (meta)sedimentary sequences,
97 ranging from Proterozoic to Neogene (Fig. 1a; Zhang et al. 2001; Deng and Wang
98 2016). The Proterozoic basement in West Qinling consists of the Paleoproterozoic
99 Qinling Group gneiss, amphibolite, and marble; the Meso-Neoproterozoic
100 Kuanping Group ophiolite unit; and the youngest Neoproterozoic sedimentary
101 units in the northeast. Another Phanerozoic cycle produced the widespread
102 sedimentary cover that accumulated continuously until the middle Triassic (Dong
103 at al. 2011; Deng et al. 2017; Meng 2017).

The West Qinling has undergone four major episodes of accretion and collision between discrete continental blocks: the Neoproterozoic southward subduction and accretion of the North China block to the North Qinling block along the Kuanping suture; the Paleozoic amalgamation between the North and South Qinling blocks along the Shangdan suture; the Triassic collisional orogeny occurred between the South Qinling block and South China block along the Mianlue suture; and post-Triassic intercontinental deformation, orogen collapse and depression (Dong and Santosh 2016; Yu et al. 2020b). The NW-oriented fold and fault systems throughout West Qinling were formed during the Triassic collisional orogeny and were reactivated during the Cenozoic by the distant effect of the collision between the India and Eurasia plates. Extensive felsic magmatism during the early Mesozoic migrated progressively eastward. Voluminous granitoid batholiths in the northern domain of the West Qinling were associated with the Triassic amalgamation between the South Qinling and South China blocks (Dong and Santosh 2016; Geng et al. 2017).

Triassic granitoids are widespread in Xiahe–Hezuo polymetallic district, situated in the northwestern most part of the West Qinling Orogen (Fig. 1). These granitic bodies usually have elliptical shapes and are discontinuously distributed in a NW–SE direction with a total exposed area of approximately 700 km^2. They generally consist of fine- to medium-grained biotite granodiorite and biotite quartz diorite, and biotite quartz diorite porphyry, intruding the Carboniferous to Triassic greenschist-facies slate and carbonate rocks. Numerous studies showed

that these granitoids were emplaced at 250 to 235 Ma and are I-type, high-K to shoshonitic, and are metaluminous to weakly peraluminous. Bulk-rock geochemical features are consistent with arc-related magmatism (Chappell and White 1974; Yang et al. 2015a, b; Qiu et al. 2016, 2018; Gou et al. 2019). Such Triassic granitoids have been recognized to be generated during the continuous northward subduction of the Paleo-Tethys oceanic slab (Qiu and Deng 2017; Yu et al. 2020a).

HOST ROCKS AND TOURMALINE TEXTURES

Sampling locality and host rock lithology

Samples investigated in this study were collected from the barren Damai stock, and the mineralized Dewulu stock and Meiwu batholith in the Xiahe–Hezuo polymetallic district (Fig. 1b). The barren Damai stock was emplaced into the Permian slate (Figs. 1, 2). It is mainly composed of fine- to medium-grained biotite granodiorite (Fig. 2a-c). Zircon in the granodiorite was dated using LA-ICPMS U-Pb to 238 Ma±4 Ma, which was interpreted as the age of emplacement (Jin et al. 2005). Quartz-tourmaline veins ranging in width from 5 to 25 cm are observed in the granodiorite with 2-3 vein sets per 10 m (Fig. 2b). No economically viable mineralization has been discovered within or around the Damai stock.

In contrast, the mineralized Dewulu stock intruded Permian clastic and

carbonate rocks, and the Early Triassic tuff (Figs. 1, 3, 4). It contains two main phases described as the biotite quartz diorite and the biotite quartz diorite porphyry that are identified by their textures. Tourmaline occurs in both phases of the Dewulu stock and the Early Triassic tuff, but is more abundant in the biotite quartz diorite porphyry (Fig. 4). The tuff and quartz diorite porphyry have zircon U–Pb ages of 252.9±4.1 Ma and 247.0±2.2 Ma (Yu et al. 2020a). The quartz diorite porphyry has been recognized as a causative intrusion associated with the Ludousou Au-Cu deposit. The estimated pre-mining resources of the Ludousou deposit included more than 8 t Au at an average grade of 3.8–5.5 g/t. Copper is currently recovered as a by-product. The ores are characterized by up to 30% tourmaline, which grew in tourmaline-quartz-chalcopyrite-pyrite-arsenopyrite veins, massive quartz-tourmaline-arsenopyrite-pyrite–chalcopyrite veins, and quartz diorite porphyry containing disseminated tourmaline (Figs. 4; Yu et al. 2020a).

The mineralized Meiwu batholith intruded into the Carboniferous and Permian meta-sedimentary rocks (Figs. 1, 5). It may be subdivided into three phases, namely the monzogranite, the biotite granodiorite, and the biotite quartz diorite. Mafic (microgranular) enclaves ranging from 5–50 cm in diameter occasionally occur in the biotite granodiorite (Fig. 5a, b). Luo et al. (2015) reported weighted mean $^{206}Pb/^{238}U$ ages of the Meiwu batholith, ranging from 244 to 240 Ma, of which the biotite granodiorite is recognized to be the causative phase for several iron skarn deposits in the vicinity. Locally, tourmaline is

169 abundant as 5 to 25 cm wide quartz-tourmaline-magnetite veins in the biotite
170 granodiorite (Fig. 5a-c).

171

172 **Tourmaline morphology**

173 **Damai tourmaline.** The tourmaline grains occurring in quartz-tourmaline
174 veins in the Damai pluton are commonly black, and appear as radial aggregates
175 (Fig. 2a, b). Tourmaline forms euhedral crystals of up to 1.5 mm in diameter and
176 coexists with quartz and minor sericite (Fig. 2e). It locally contains quartz
177 inclusions (Fig. 2e) and replaces plagioclase (Fig. 2d, e). Optical microscopy
178 reveals that the tourmaline exhibits a homogeneous light green center and a thick
179 (50–300 μm) brown rim with oscillatory zoning perpendicular to the c–axis (Fig.
180 2d, e).

181 **Dewulu tourmaline.** Barren tourmaline breccia bodies (Fig. 3) and
182 mineralized tourmaline veins (Fig. 4) are found in the Dewulu stock. The host
183 rocks of the breccia bodies are felsic to intermediate volcanic rocks. The breccia
184 fragments vary in size from 1 to 20 cm in diameter (Fig. 3a). Most of the
185 fragments are tuffaceous gravel and enveloped by a ~0.5 cm wide fine-grained
186 tourmaline-quartz rim (Fig. 3a-c). These tourmaline grains mostly vary from 30
187 to 60 μm in diameter and exhibit moderate pleochroism with small cyan centers
188 and thin brown rims (Fig. 3c). The matrix comprises quartz, plagioclase, sericite,
189 and disseminated tourmaline, and cements fragments of tuff breccia and sickle

quartz (Fig. 3b). The tourmaline grains in the matrix are commonly less than 20 μm in diameter. No sulfide minerals are found in the tourmaline breccia bodies.

The mineralized tourmaline veins are distinguished from tourmaline in the breccia by the mineral assemblages and textural occurrence of tourmaline (Fig. 4). The tourmaline veins occur in the biotite quartz diorite porphyry and are the main ores in the Ludousou Au-Cu deposit, with an average gold grade of 3.8–5.5 g/t (Yu et al. 2020a). The vein type tourmaline may be further divided into three styles, namely the tourmaline-quartz vein (Fig. 4a, b), the massive quartz-tourmaline vein (Fig. 4c, d), and the disseminated tourmaline (Fig. 4a, b, e). Tourmaline-quartz veins are typically 5–40-cm-wide and commonly occur along joints of host rocks (Fig. 4a, b). They consist mostly of tourmaline and quartz, with chalcopyrite, pyrite, and lesser arsenopyrite and rutile (Fig. 4j). The massive tourmalines are distributed in the middle part of the Dewulu stock and may contain silicified porphyry xenoliths (Fig. 4c). They coexist with abundant arsenopyrite and lesser pyrite and chalcopyrite (Fig. 4d, k). The volume of massive tourmaline, occurring over an area of 50 × 100 m hosts the major gold and copper resources of the Ludousou deposit (Fig. 4c, d). The disseminated tourmalines are commonly hosted by the quartz diorite porphyry proximal to tourmaline-quartz veins and massive quartz-tourmaline veins (Fig. 4a, b, e). The tourmaline grains coexist with quartz, sericite, rutile, and coarse-grained pyrite (Fig. 4f, i).

All three styles of the vein type tourmaline coexist with quartz, chalcopyrite,

pyrite, arsenopyrite, with minor rutile and sericite (Fig. 4). Compared with fine-grained tourmaline in the tourmaline breccia bodies, the tourmaline crystals in the biotite quartz diorite porphyry are much larger, mostly ranging from 200 μm up to 1500 μm in diameter (Fig. 4). The tourmalines are characterized by moderate pleochroism and well-developed color growth zoning with light green cores and thick light green to brown rims (Fig. 4g-h). Some grains have sector zoned cores, although the majority have homogeneous cores surrounded by oscillatory zoned rims (Fig. 4i, k, l).

Meiwu tourmaline. The tourmaline grains occur in 5−15 cm wide quartz-tourmaline-magnetite veins in the Meiwu pluton (Fig. 5a-c). The euhedral homogeneous crystals are black in hand specimen, and are much smaller than other occurrences, mostly ranging from 50 to 80 μm in diameter (Fig. 5d). Tourmaline coexists with quartz and magnetite, and replaces plagioclase (Fig. 5d-f).

ANALYTICAL METHODS AND DATA REPRESENTATION

Sample preparation

Doubly polished thin section samples were prepared for petrographic analysis. Representative tourmaline grains were located on each thin section, and subsequently 1.5 × 1.5 cm squares with each tourmaline texture of interest were extracted and mounted in epoxy for in situ micro-analysis of major elements and

boron isotope analyses using EPMA and LA-MC-ICP-MS. The sampling description and locality are given in Supplementary Table 1.

Electron-probe micro-analysis of tourmaline

The major element compositions of 55 tourmaline grains from Damai, Meiwu, and Dewulu were determined using a JEOL JXA-8100 electron probe micro-analyzer equipped with four wavelength dispersive-type spectrometers at the Institute of Mineral Resources, Chinese Academy of Geological Sciences (CAGS), Beijing, China, using analytical procedures given in Huang et al. (2016). The analytical data are presented in Supplementary Table 2. Tourmaline structural formulae were calculated by normalizing to 15 cations in the tetrahedral and octahedral sites (T + Z + Y), and assuming stoichiometric compositions with regard to three B atoms per formula unit (a.p.f.u.), four (OH+F) a.p.f.u. (Henry and Dutrow 1996).

LA-MC-ICP-MS boron isotope analysis of tourmaline

In situ tourmaline boron isotope analyses were carried out on the same 55 tourmaline grains over the top of the same points analyzed by EPMA. Boron isotopic compositions of tourmaline were conducted by LA-MC-ICP-MS at the State Key Laboratory for Mineral Deposits Research at the Nanjing University, China. A Neptune Plus MC-ICP-MS (Thermo Finnigan) coupled with a

NewWave UP193 LA system were used. A laser repetition rate of 5 Hz at 11 J/m^2 was used for ablating tourmalines with a 60 μm spot. Detailed operating conditions of the laser ablation system and the MC-ICP-MS instrument and data reduction are provided in Yang et al. (2015). The Boron isotope compositions are expressed in the standard delta notation ($\delta^{11}B = (R_{sample}/R_{standard}-1)\times1000$), where R is the ratio of $^{11}B/^{10}B$, reported as permil (‰) deviations from the NIST SRM-951 international standard (Catanzaro et al., 1970). Mass bias of the instrument and the fractionation of isotopes were calibrated in this study using the standard-sample-bracketing (SSB) method. The tourmaline IAEA B4 ($\delta^{11}B = -8.71$ ‰; Tonarini et al. 2003) was used as the primary standard. The reproducibility and accuracy of the procedure was checked by repeated measurement of the Tourmaline reference materials IMR RB1 of $\delta^{11}B$=-13.86±0.73 (2σ, n=70), which are consistent with the recommended values of $\delta^{11}B$=-12.96±0.97 (2σ, n=57; Hou et al. 2010). The boron isotope data are given in Supplementary Table 3.

RESULTS

Chemical composition of tourmaline

The analysis totals for tourmaline are less than 90 wt.% because EPMA cannot determine B, H_2O, and Li (Supplementary Table 2). Overall, no systematic trends in major element abundances from cores to rims are observed in the Damai and Dewulu tourmalines (Figs. 6, 7). Meiwu tourmalines are homogeneous

without compositional zoning (Figs. 5-7).

Most of the tourmalines described in this study belong to the alkali group in the Ca-X-site vacancy-Na(+K) ternary diagrams (Fig. 6a). In the ternary Al-Fe-Mg diagram of Henry and Guidotti (1985), the Damai tourmalines plot in field 2, suggesting that they formed in an environment similar to Li-poor granitoids and associated pegmatites and aplites (Fig. 6b). The other tourmaline grains at Dewulu and Meiwu fall mainly within field 5 in the ternary Al–Fe–Mg diagram, similar to metapelite and metapsammite samples lacking Al-saturating phases (Fig. 6b).

The Damai tourmalines have Mg/(Fe+Mg) and Na/(Na+Ca) ratios between 0.32 and 0.44, and 0.82 to 0.93, and plot in the schorl (Fe-rich) field (Fig. 7a). These Damai tourmalines have lower and less variable Ca contents (Fig. 7b). Plots of Al versus Fe and Na versus Al indicate the influence of $^{X}\square Al(NaMg)_{-1}$ substitution mechanism for the Damai tourmalines (Fig. 7c-e). Tourmalines in the tuffaceous breccia body at Dewulu have Mg/(Fe+Mg) and Na/(Na+Ca) ratios from 0.49 to 0.71 and 0.39 to 0.76. Nearly all of the fine-grained tourmalines plot in the dravite field (Fig. 7a). Plots of Al versus Fe and Mg versus Fe suggest that the $Fe^{2+}Mg_{-1}$ substitution plays an important role for the tourmaline found in the tuffaceous breccia body (Fig. 7c, d). Tourmaline grains from the tourmaline-quartz, massive tourmaline, and disseminated tourmaline samples at Dewulu exhibit similar compositions. They have Mg/(Fe+Mg) and Na/(Na+Ca) ratios from 0.40 to 0.83 and 0.54 to 0.90 respectively, and plot in the schorl (Fe-rich) to

297 dravite (Mg-rich) field (Fig. 7a). Plots of Al versus Fe and Mg versus Fe (Fig. 7c,
298 d) document the influence of $Fe^{2+}Mg_{-1}$ and $Fe^{3+}Al_{-1}$ substitution mechanisms for
299 the tourmaline-quartz, massive tourmaline, and disseminated tourmaline
300 samples. The Meiwu tourmalines belong to the Mg-rich dravite group with
301 Mg/(Fe+Mg) and Na/(Na+Ca) ratios from 0.60 to 0.82 and 0.61 to 0.90
302 respectively (Fig. 7a) and variable Ca contents (0.09 to 0.36 a.p.f.u) (Fig. 7b). The
303 variation of Al-contents in tourmalines may be controlled by some substitution of
304 Fe^{3+} in accordance with the $Fe^{3+}Al_{-1}$ (Fig. 7c).

305

306 **Boron isotopic composition of tourmaline**

307 **Damai tourmaline.** The $\delta^{11}B$ values of the Damai tourmalines range from
308 −9.1 to −7.9 ‰. No systematic variations in $\delta^{11}B$ values from cores to rims were
309 observed (Figs. 2e, 8).

310 **Dewulu tourmaline.** The tourmalines from Dewulu have $\delta^{11}B$ values ranging
311 from −10.8 to −4.0 ‰. The tourmalines in the breccia body yield the highest $\delta^{11}B$
312 values, ranging from −6.6 to −4.0 ‰ (Figs. 3c, 8). The tourmalines in the
313 tourmaline-quartz, massive tourmaline, and disseminated tourmaline samples
314 have $\delta^{11}B$ values of −10.8 to −5.6 ‰, −9.6 to −6.2 ‰, and −9.6 to −7.1 ‰,
315 respectively. For those tourmalines exhibiting oscillatory zoning texture, the core
316 generally yields higher $\delta^{11}B$ values than rims (Figs. 4k, i, 8).

317 **Meiwu tourmaline.** The Meiwu tourmalines have a narrow range of $\delta^{11}B$

values of −11.4 to −10.0 ‰. They show no systematic variations in $\delta^{11}B$ values within individual tourmaline grains (Fig. 8).

DISCUSSION

Origins of tourmaline

Fine-grained tourmaline that are common in the Dewulu tuff occurring in the breccia matrix and quartz-tourmaline rims (Fig. 3a), have textures similar to those formed in breccia pipes (Pirajno et al. 2000; Dill et al. 2012). The textures suggest formation of breccia that caused expulsion of accumulating fluids and gases from the magma (high-pressure regime) into the fractures (low pressure regime) within the host-rock tuff. It has been established that the major element composition of tourmaline in hydrothermal systems may be influenced, in part, by host rock composition depending on the water/rock ratios (e.g., Henry and Guidotti 1985; Pal et al. 2010; Yang et al. 2015). The tourmalines display high Mg/(Mg+Fe) and Ca values, and low Na/(Na+Ca) values, comparable to those of the host Dewulu tuff, and thus attest to tourmaline growth that inherited the composition of the original magmatic–hydrothermal fluid (Fig. 7a; Yang et al. 2015; Deng et al. 2020). Such textural and geochemical characteristics suggested that tourmaline which filled the newly formed open spaces during brecciation precipitated by magma-fluid immiscibility during a transition from magmatic to hydrothermal process (Dill et al. 2012).

Other tourmalines in the Xiahe-Hezuo polymetallic district are represented by euhedral to subhedral grains that coexist with quartz and sericite in quartz-tourmaline veins with sharp contacts toward host granitoids (Figs. 2, 4, 5). Plagioclase is replaced by disseminated tourmalines in host granitoids near the vein, leaving only residual plagioclase grains (Figs. 2d, 4f), or fragmenting the plagioclase grains into several pieces (Fig. 5d). Taking into consideration that hydrothermal minerals such as quartz, tourmaline, and sericite occur in the veins, sharp contact relationships between the quartz-tourmaline vein and wall rock, and the replacement texture suggest that all tourmaline crystallized from B-rich hydrothermal fluids, and not from a B-rich melt (Yang et al. 2012; Yang et al. 2015 and references therein).

The Dewulu and Meiwu tourmalines in quartz-tourmaline veins have wide ranges of major element compositions (Fig. 7a). This may be attributed to the dissolution of Mg- and Ca- rich minerals, such as biotite, plagioclase, and amphibole, as water/rock ratios increased during tourmaline crystallization (Fig. 4f, 5d; Huang et al. 2016). The massive quartz-tourmaline-sulfide veins without any biotite, plagioclase, and amphibole relicts in the Dewulu quartz diorite porphyry show high Mg and Ca values (Figs. 4d, g, h, 7a, b). Yang et al. (2012) pointed out that, when fluid becomes dominant, the silicate minerals of the host rock may provide the requisite Mg–Ca–Al constituents necessary for the B-rich fluids to crystallize extensive tourmaline. The release of iron from biotite and amphibole also increases iron concentrations in hydrothermal fluids (Pal et al.

2010; Yang et al. 2012; Hong et al. 2017; Qiu et al. 2020), and promotes precipitation of sulfides and magnetite in the Dewulu and Meiwu quartz-tourmaline veins (Figs. 4g-j, 5e, f). The slightly higher Na/(Na+Ca) and lower Ca values in the Meiwu tourmaline compared to that of Dewulu (Fig. 7a, b) suggests additional controls on the Meiwu tourmaline composition (Pal et al. 2010). Such controls are probably ascribed to the formation of iron skarn deposits in Meiwu during which Ca-bearing minerals crystallized, depleting Ca in the fluids, which led to high Na/(Na+Ca) values in the tourmalines (Fig. 7).

The Damai tourmalines in the quartz-tourmaline vein display distinct major element compositions, low Mg and Ca values, and high Al and Fe values, compared to the host Damai stock and tourmalines at Dewulu and Meiwu (Fig. 7a). The geochemical homogeneity and absence of textures attributable to post-crystallization alteration suggest that formation of the Damai tourmaline was from a single fluid with limited fluid-rock reaction. The Damai tourmalines, corresponding to tourmalines from Li-poor granitoids (Fig. 6b), are therefore most likely precipitated from a hydrothermal fluid that evolved from granite, without assimilation of the surrounding rocks.

Source and evolution of fluids

Tourmalines in tourmaline-quartz breccias from Dewulu likely reflect the original magmatic–hydrothermal fluids. The $\delta^{11}B$ of the fine-grained tourmalines

(−6.6 ‰ to −4.0 ‰) therefore should approximate that of the parental granitic magma. Such values are slightly higher than that of typical continental crust (−13 ‰ to −7 ‰), but are consistent with ~90 % of values reported worldwide for granites and pegmatites (−16 ‰ to −4 ‰), granite-related veins (−24 ‰ to −4 ‰), and mid-ocean ridge basalt and mantle (−10 ‰ to −1 ‰) (Fig. 8; Marschall and Jiang 2011; van Hinsberg et al. 2011). Consequently, the boron isotope signature is consistent with derivation from continental crust with lesser mantle contribution. This finding is consistent with the geochemical and Sr-Nd isotopic composition of granitoids in the Xiahe–Hezuo polymetallic district, indicating that the magma was derived from partial melting of mafic lower crust and enriched lithospheric mantle (Luo et al. 2015; Qiu and Deng 2017).

Most of the tourmaline grains in quartz-tourmaline veins from Dewulu display oscillatory zoning textures (Fig. 4g-i, k, l). Their cores generally display heavier ^{11}B values, ranging from −7.1 ‰ to −5.6 ‰ (Fig. 8), indicating that the tourmalines in quartz-tourmaline veins were inherited from magmatic–hydrothermal fluids that precipitated the fine-grained tourmaline in tuffaceous breccia. In contrast, a significant negative shift of ^{11}B was observed in the rims (Fig. 8). Two different models have been proposed to explain the isotopic variations between cores and rims of single tourmaline grains: (1) mixing of fluids from multiple sources; and (2) evolution of a fluid from a single source induced by temperature changes, fluid unmixing, crystallization, and degassing (e.g., Smith and Yardley 1996; Huang et al. 2016; Albert et al. 2018). The

tourmaline from Dewulu shows similar ranges of major element compositions, which excludes the possibility that the tourmalines with oscillatory zoning texture formed from multiple sources (Figs. 6, 7; Yang et al. 2015; Huang et al. 2016). Consequently, the boron isotope variation most likely resulted from evolution of the fluid-geochemistry. A change in temperature is obviously not sufficient to result in such a large isotope variation (Fig. 9; Meyer et al. 2008; Huang et al. 2016) and no evidence illustrating fluids unmixing was observed in previous or current studies (Wang 2004; Jin 2013). The possibility that the isotope variations resulted from continuous tourmaline crystallization is therefore excluded. If this were the case, the tourmaline should have gradually heavier isotope values from cores to rims, because ^{10}B partitions preferentially into the tourmaline relative to a liquid phase, leading to an increase in the $\delta^{11}B$ of the residual fluid (Palmer et al. 1992; Meyer et al. 2008; Albert et al. 2018). Experimental studies have shown that the escaping fluid and/or vapor will carry ^{11}B and produce a significant enrichment of ^{10}B in the residual phase during degassing processes (Jiang and Palmer 1998; Albert et al. 2018). Hence, it suggests that continuous vapor loss attributed to brecciation was induced by liquid-gas immiscibility and gave rise to the significant isotope shift between cores and rims of the tourmalines at Dewulu. The significant B isotope fractionation reflected in the decrease in $\delta^{11}B$ values from cores (−5.6 ‰) to rims (−10.7 ‰), may be modeled using Rayleigh fractionation, and indicates that a relatively large proportion of the fractionation is attributable to degassing ($F<0.2$) during fluid evolution in Dewulu (Fig. 9;

426 Leeman et al. 1992; Huang et al. 2016).

427 The substitution mechanisms in the crystallization of the tourmaline rims in
428 the vein type tourmaline are $Fe^{3+}Al_{-1}$ and $Fe^{2+}Mg_{-1}$, compared to tourmalines in
429 the tuffaceous breccias, which are dominated by the substitution mechanism of
430 $Fe^{2+}Mg_{-1}$ (Fig. 7c, d). This indicates a higher oxygen fugacity fluid forming the
431 vein type tourmaline. Yang et al. (2002) and Pal et al. (2010) proposed that
432 continuous degassing may cause loss of H_2 in the liquid phase, and increase
433 oxygen fugacity of the residual liquid. The substitution mechanism of $Fe^{3+}Al_{-1}$,
434 therefore, is interpreted as a result of the degassing. Moreover, most of the
435 tourmalines in Meiwu display a good correlation of Al with Fe, suggesting a
436 substitution of Al^{3+} by Fe^{3+} (Fig. 7c, d). This implies that the fluids precipitating
437 Meiwu tourmalines are oxidized (>FMQ), consistent with the observation that
438 large amounts of magnetite coexist with tourmaline in Meiwu (Fig. 5e, f; Fuchs
439 et al. 1998; Roda-Robles et al. 2015).

440 Although there is little evidence for intra-crystal boron isotopic variations in
441 Meiwu tourmalines because of their tiny crystal size, the lightest $\delta^{11}B$ values
442 (−11 ‰) indicate that significant degassing occurred before the tourmaline
443 crystallized (Fig. 8). The high Al contents in Damai tourmaline, in excess of the
444 six cations per formula unit for ideal schorl–dravite, correlate negatively with Na.
445 This suggests that excess Al is charge-balanced by the substitution $^{X}\square Al(NaMg)_{-1}$
446 rather than $AlO(Mg(OH))_{-1}$ (Fig. 7e; Baksheev et al. 2015). Henry and Dutrow
447 (2012) proposed that high proportions of the X-site vacancy in tourmaline are

448 caused by low Na content (1.8 wt.% NaCl eq.) of mineralizing fluids. The strong
449 linear substitution between (^{X}□Al) and (NaMg) also supports this proposition
450 (Fig. 7e).

451

452 **Tracer for magmatic-hydrothermal mineralization**

453 Geochemical indicators, including substitution mechanisms of major
454 elements, Fe content, and shift of δ^{11}B values in tourmaline clearly distinguish the
455 mineralized intrusion (Dewulu and Meiwu) from the barren granite (Damai) in
456 the Xiahe-Hezuo polymetallic district.

457 The substitution mechanisms of major elements reflect the oxygen fugacity
458 and salinity of fluids. A good correlation of Al with Fe at Dewulu and Meiwu,
459 indicating substitution of Al^{3+} by Fe^{3+}, is suggestive of oxidized fluids. On the
460 contrary, a substitution of $Fe^{2+}Mg_{-1}$ at Damai implies a reduced fluid (<MW). An
461 important feature of the magmatic-hydrothermal deposits is that the primary fluid
462 had a relatively low oxygen fugacity that plots in the pyrite and chalcopyrite
463 stability field. The substitution mechanism changed during growth of the
464 tourmaline from Mg^{2+} by Fe^{2+} to Al^{3+} by Fe^{3+}, suggesting a sharp increase of
465 oxygen fugacity. This facilitates the reduction of metal solubility and promotes
466 metal deposition. (e.g., Williams-Jones 2009). The substitution mechanism of
467 $Fe^{3+}Al_{-1}$, therefore, has a positive impact on mineralization. However, $Fe^{2+}Mg_{-1}$
468 and ^{X}□$Al(NaMg)_{-1}$ substitutions suggest that the fluids may be reduced (<MW)

and of low salinity (1.8 wt.% NaCl eq.) (Fuchs et al. 1998; Henry and Dutrow 2012; Roda-Robles et al. 2015). Yardley (2005) described the importance of aqueous chlorite complexes for producing economic deposits because these complexes dominante the transport of metals in magmatic hydrothermal fluids. This implies that low salinity magmatic fluids are less likely to transport dissolved-metals budgets sufficient to produce economic deposits. This implies that the fluids crystallizing tourmalines with $Fe^{2+}Mg_{-1}$ and $^{X}\square Al(NaMg)_{-1}$ substitutions have low ore-forming potential. The Fe value in tourmaline also serves as a good indicator for mineralization. Experimental petrology studies indicate that Fe was released from biotite decomposition into B-rich fluids to form tourmaline and iron sulfides or oxides during fluid-rock interaction (Cheng et al. 2020). As a result, low Fe content in tourmalines at Dewulu and Meiwu reflect high abundances of iron sulfides or oxides, indicating a greater ore-forming potential. In contrast, all the tourmaline grains at Damai exhibiting high Fe contents, reflecting the lack of significant metal-enrichment in the intrusion. The shift of $\delta^{11}B$ values is another indicator that may reflect the degree of degassing. Degassing may increase the oxygen fugacity of the fluids by loss of H_2, and also concentrate metallogenic elements. A significant negative shift of ^{11}B observed in most of the tourmaline grains at Dewulu is likely to signify a distinct degassing event (Fig. 9). The Dewulu granitoids crystallized from magmas that were chemically reducing and characterized by low oxygen fugacity (Jin et al. 2017; Sui et al. 2018), which are not conducive to the formation of magmatic hydrothermal

deposits (Sun et al. 2015; Yu et al. 2019). Yet, such degassing processes increased the oxygen fugacity and the concentrations of metallogenic elements in the fluid, contributing to formation of the Dewulu deposit. The shift of $\delta^{11}B$ values of tourmalines, therefore, may be used to distinguish metal fertility from granitoid to granitoid.

IMPLICATIONS

Geochemical characteristics described above highlight the potential of tourmaline as a tracer of magmatic-hydrothermal processes and mineralization. Both major element and isotope compositions in tourmaline change as physicochemical conditions of magmatic-hydrothermal fluids vary. For tourmalines from causative granitoids, their major element compositions are controlled by $Fe^{3+}Al_{-1}$ substitution, suggesting that fluids became more oxidized due to the liquid-gas immiscibility processes. Also the large negative shift of $\delta^{11}B$ from cores to rims documented in these tourmalines reflects the immiscibility. Rayleigh fractionation models of $\delta^{11}B$ may effectively reflect the degree of boron degassing, which is directly related to decreasing metal solubility and promotes the formation of ores. In contrast, $^{X}\square Al(NaMg)_{-1}$ is the dominant substitution mechanism for tourmalines in barren granitoids owing to crystallization in the presence of reduced fluids with low salinity. Such magmatic-hydrothermal fluids cannot transport enough metal to give rise to economic mineralization. Diagrams that plot Al/Fe, Mg/Fe, Al/Na, Fe values, and shift of $\delta^{11}B$ values in tourmaline

513 are proposed as discriminators to explore ore-bearing granites from barren
514 intrusions.

515

516 **ACKNOWLEDGEMENTS**

517 Robert Trumbull at GFZ and Ryan Taylor at USGS are acknowledged for
518 thoughtful discussions. We appreciate Editor Don Baker, the associate editor Jade
519 Star Lackey, and two reviewers, Prof. Mona-Liza C Sirbescu and Dr. James
520 Maner, for their critical, careful, and very constructive reviews that helped to
521 improve the clarity and interpretations of the original draft. This research was
522 financially supported by the National Natural Science Foundation (41702069,
523 91962106), the National Key Research Program (2019YFA0708603), the
524 Fundamental Research Funds for the Central Universities (2652018125), the State
525 Key Laboratory for Mineral Deposits Research (2017-LAMD-K05), the State Key
526 Laboratory of Ore Deposit Geochemistry (201704), and the 111 Project of
527 Ministry of Science and Technology of China (BP0719021).

528

529 **REFERENCES CITED**

530 Albert, C., Lana, C., Gerdes, A., Schannor, M., Narduzzi, F., and Queiroga, G.
531 (2018) Archean magmatic-hydrothermal fluid evolution in the Quadrilátero
532 Ferrífero (SE Brazil) documented by B isotopes (LA MC-ICPMS) in
533 tourmaline. Economic Geology, 481, 95-109.

534 Baksheev, I.A., Prokofiev, V.Y., Trumbull, R.B., Wiedenbeck, M., and Yapaskurt,
535 V.O. (2015) Geochemical evolution of tourmaline in the Darasun gold
536 district, Transbaikal region, Russia: evidence from chemical and boron
537 isotopic compositions. Mineralium Deposita, 50(1), 125-138.

538 Catanzaro, E.J., Champion, C.E., Garner, E.L., Marinenko, G., Sappenfield, K.
539 M., and Shields, W.R. (1970) Boric acid: isotopic and assay standard
540 reference materials, National Bureau of Standards. Institute for Materials
541 Research, Maryland, USA.

542 Chappell, B.W. and White, A.J.R. (1974) Two Contrasting Granite Types. Pacific
543 Geology, 8, 173-174.

544 Cheng, L., Zhang, C., and Yang, X. (2020). Petrogenesis of deformed tourmaline
545 leucogranite in the Gurla Mandhata metamorphic core complex,
546 Southwestern Tibet. Lithos, 105533.

547 Dill, H.G., Garrido, M.M., Melcher, F., Gomez, M.C., and Luna, L.I., (2012)
548 Depth-related variation of tourmaline in the breccia pipe of the San Jorge
549 porphyry copper deposit, Mendoza, Argentina. Ore Geology Reviews, 48,
550 271-277.

551 Deng, J., and Wang, Q.F. (2016) Gold mineralization in China: Metallogenic
552 provinces, deposit types and tectonic framework. Gondwana Research, 36,
553 219-274.

554 Deng, J., Wang, Q.F. and Li, G.J. (2017) Tectonic evolution, superimposed
555 orogeny, and composite metallogenic system in China. Gondwana Research,
556 50, 216-266.

557 Deng, J., Wang, C.M., Bagas, L., Santosh, M., and Yao, E.Y. (2018) Crustal
558 architecture and metallogenesis in the south-eastern North China Craton.
559 Earth-science reviews, 182, 251-272.

560 Deng, J., Qiu, K.F., Wang, Q.F., Goldfarb, R.J., Yang, L.Q., Zi, J.W., Geng, J.Z.,
561 and Ma, Y., (2020) In-situ dating of hydrothermal monazite and implications
562 on the geodynamic controls of ore formation in the Jiaodong gold province,
563 Eastern China. Economic Geology, 115, 671-685

564 Dong, Y.P., Zhang, G.W., Neubauer, F., Liu, X.M., Genser, J. and Hauzenberger,
565 C. (2011) Tectonic evolution of the Qinling orogen, China: review and
566 synthesis. Journal of Asian Earth Sciences, 41, 213-237.

567 Dong, Y.P., and Santosh, M. (2016) Tectonic architecture and multiple orogeny of
568 the Qinling Orogenic Belt, Central China. Gondwana Research, 29(1), 1-40.

569 Dyar, M.D., Wiedenbeck, M., Robertson, D., Cross, L.R., Delaney, J.S.,
570 Ferguson, K., Francis, C.A., Grew, E.S., Guidotti, C.V., Hervig, R.L.,
571 Hughes, J.M., Husler, J., Leeman, W., McGuire, A.V., Rhede, D., Rothe, H.,
572 Paul, R.L., Richards, I., and Yates, M. (2001) Reference minerals for the
573 microanalysis of light elements. Geostandards Newsletter, 25(2-3), 441-463.

574 Fuchs, Y., Lagache, M., and Linares, J. (1998). Fe-tourmaline synthesis under
575 different T and f O2 conditions. American Mineralogist, 83(5-6), 525-534.

576 Garda, G.M., Trumbull, R.B., Beljavskis, P. and Wiedenbeck, M. (2009) Boron
577 isotope composition of tourmalinite and vein tourmalines associated with
578 gold mineralization, Serra do Itaberaba Group, central Ribeira Belt, SE
579 Brazil. Chemical Geology, 264(1-4), 207-220.

580 Geng, J.Z., Qiu, K.F., Gou, Z.Y., and Yu, H.C. (2017) Tectonic regime
581 switchover of Triassic Western Qinling Orogen: Constraints from LA-ICP-
582 MS zircon U–Pb geochronology and Lu–Hf isotope of Dangchuan intrusive
583 complex in Gansu, China. Geochemistry, 77(4), 637-651.

584 Gou, Z.Y., Yu, H.C., Qiu, K.F., Geng, J.Z., Wu, M.Q., Wang, Y.G., Yu, M.H.,
585 and Li, J. (2019) Petrogenesis of ore-hosting diorite in the Zaorendao gold
586 deposit at the Tongren-Xiahe-Hezuo polymetallic district, West Qinling,
587 China. Minerals, 9(2), 76.

588 Hawthorne, F.C., and Henry, D.J. (1999) Classification of the minerals of the
589 tourmaline group. EUROPEAN JOURNAL OF MINERALOGY-
590 STUTTGART-, 11, 201-216.

591 Henry, D.J., and Dutrow, B.L. (1996) Metamorphic tourmaline and its petrologic
592 applications. In: Grew ES, Anovitz LM (eds) Boron: mineraqlogy, petrology
593 and geochemistry. Mineralogical Society of America, Washington, D.C.,
594 Reviews in mineralogy, 33, 503-557.

595 Henry, D.J., and Dutrow, B.L. (2012) Tourmaline at diagenetic to low-grade
596 metamorphic conditions: Its petrologic applicability. Lithos, 154, 16-32.

597 Henry, D.J., and Guidotti, C.V. (1985) Tourmaline as a petrogenetic indicator
598 mineral: an example from the staurolite-grade metapelites of NW Maine.
599 American mineralogist, 70 (1-2), 1-15.

600 Hong, W., Cooke, D.R., Zhang, L., Fox, N., and Thompson, J. (2017)
601 Tourmaline-rich features in the Heemskirk and Pieman Heads granites from
602 western Tasmania, Australia: Characteristics, origins, and implications for
603 tin mineralization. American mineralogist, 102(4), 876-899.

604 Hou, K., Li, Y., Xiao, Y., Liu, F., and Tian, Y. (2010) In situ boron isotope
605 measurements of natural geological materials by LA-MC-ICP-MS. Chinese
606 Science Bulletin, 55(29), 3305-3311.

607 Huang, S.Q., Song, Y.C., Hou, Z.Q. and Xue, C.D. (2016) Chemical and stable
608 isotopic (B, H, and O) compositions of tourmaline in the Maocaoping vein-
609 type Cu deposit, western Yunnan, China: Constraints on fluid source and
610 evolution. Chemical Geology, 439, 173-188.

611 Jiang, S.Y. and Palmer, M.R. (1998) Boron isotope systematics of tourmaline
612 from granites and pegmatites; a synthesis. European Journal of Mineralogy,
613 10(6), 1253-1265.

614 Jiang, S.Y., Palmer, M.R., and Yeats, C.J. (2002) Chemical and boron isotopic
615 compositions of tourmaline from the Archean Big Bell and Mount Gibson

616 gold deposits, Murchison Province, Yilgarn craton, Western Australia.
617 Chemical Geology, 188(3-4), 229-247.

618 Jiang, S.Y., Radvanec, M., Nakamura, E., Palmer, M., Kobayashi, K., Zhao,
619 H.X., and Zhao, K.D. (2008) Chemical and boron isotopic variations of
620 tourmaline in the Hnilec granite-related hydrothermal system, Slovakia:
621 Constraints on magmatic and metamorphic fluid evolution. Lithos, 106(1-2),
622 1-11.

623 Jin, W.J., Zhang, Q., He, D.F., and Jia, X.Q. (2005) SHRIMP dating of adakites
624 in western Qinling and their implications. Acta Petrologica Sinica, 21(3),
625 959-966 (in Chinese with English abstract).

626 Jin, X.Y. (2013). Genesis of the Laodou gold deposit, Xiahe-Hezuo area, west
627 Qinling orogen: Constraints from the geochemistry and isotopic
628 geochronology. Master's Thesis, China University of Geosciences, 1-129 (in
629 Chinese with English abstract).

630 Jin, X.Y., Li, J.W., Hofstra, A.H., and Sui, J.X. (2017) Magmatic-hydrothermal
631 origin of the early Triassic Laodou lode gold deposit in the Xiahe-Hezuo
632 district, West Qinling orogen, China: implications for gold metallogeny.
633 Mineralium Deposita, 52, 883-902

634 Leeman, W.P., Vocke, R.D., and McKibben, M.A. (1992) Boron isotopic
635 fractionation between coexisting vapor and liquid in natural geothermal
636 systems. Water-Rock Interaction, 1, 1007-1010.

637 Li, J.W., Sui, J.X., Jin, X.Y., Wen, G., Chang, J., Zhu, R., Zhan, H.Y., and Wu,
638 W.H. (2019) The intrusion-related gold deposits in the Xiahe-Hezuo district,
639 West Qinling Orogen: geodynamic setting and exploration potienal.
640 Geoscience Frontiers, 26(5), 17-32 (in Chinese with English abstract)

641 Luo, B.J., Zhang, H.F., Xu, W.C., Yang, H., Zhao, J.H., Guo, L., Zhang, L.Q.,
642 Tao, L., Pan, F.B., and Gao, Z. (2018) The magmatic plumbing system for
643 Mesozoic high-Mg andesites, garnet-bearing dacites and porphyries, rhyolites
644 and leucogranites from West Qinling, Central China. Journal of Petrology,
645 59(3), 447-482.

646 Luo, B.J., Zhang, H.F., Xu, W.C., Guo, L., Pan, F.B., and Yang, H. (2015) The
647 Middle Triassic Meiwu Batholith, West Qinling, Central China: implications
648 for the evolution of compositional diversity in a composite Batholith.
649 Journal of Petrology, 56(6), 1139-1172.

650 Maner IV, J.L., London, D., and Icenhower, J.P. (2019). Enrichment of
651 manganese to spessartine saturation in granite-pegmatite systems. American
652 Mineralogist: Journal of Earth and Planetary Materials, 104(11), 1625-1637.

653 Marschall, H.R., and Jiang, S.Y. (2011) Tourmaline isotopes: no element left
654 behind. Elements, 7(5), 313-319.

655 Meng, Q.R. (2017) Origin of the Qinling Mountains (in Chinese). Scientia Sinica
656 Terrae, 47, 412-420, doi: 10.1360/N072016-00422

Meyer, C., Wunder, B., Meixner, A., Romer, R.L., and Heinrich, W. (2008) Boron-isotope fractionation between tourmaline and fluid: an experimental re-investigation. Contributions to Mineralogy and Petrology, 156(2), 259-267.

Mlynarczyk, M.S., and Williams-Jones, A.E. (2006) Zoned tourmaline associated with cassiterite: implications for fluid evolution and tin mineralization in the San Rafael Sn-Cu deposit, southeastern Peru. The Canadian Mineralogist, 44(2), 347-365.

Pal, D.C., Trumbull, R.B., and Wiedenbeck, M. (2010) Chemical and boron isotope compositions of tourmaline from the Jaduguda U (-Cu-Fe) deposit, Singhbhum shear zone, India: implications for the sources and evolution of mineralizing fluids. Chemical Geology, 277(3-4), 245-260.

Palmer, M.R., London, D., VI, G.M., and Babb, H.A. (1992) Experimental determination of fractionation of $^{11}B/^{10}B$ between tourmaline and aqueous vapor: A temperature-and pressure-dependent isotopic system. Chemical Geology: Isotope Geoscience section, 101(1-2), 123-129.

Pirajno, F., Phillips, D., and Armstrong, R.A. (2000) Volcanology and eruptive histories of the Erongo volcanic complex and the Paresis igneous complex, Namibia: implications for mineral deposit styles. Communications of the Geological Survey of Namibia, 12, 301-312.

Qiu, K.F., Taylor, R.D., Song, Y.H., Yu, H.C., Song, K.R., and Li, N. (2016) Geologic and geochemical insights into the formation of the Taiyangshan

porphyry copper-molybdenum deposit, Western Qinling Orogenic Belt, China. Gondwana Research, 35, 40-58.

Qiu, K.F., and Deng, J. (2017) Petrogenesis of granitoids in the Dewulu skarn copper deposit: implications for the evolution of the Paleotethys ocean and mineralization in Western Qinling, China. Ore Geology Reviews, 90, 1078-1098.

Qiu, K.F., Yu, H.C., Gou, Z.Y., Liang, Z.L., Zhang, J.L., and Zhu, R. (2018) Nature and origin of Triassic igneous activity in the Western Qinling Orogen: the Wenquan composite pluton example. International Geology Review, 60(2), 242-266.

Qiu, K.F., Yu, H.C., Deng, J., McIntire, D., Gou, Z.Y., Geng, J.Z., Chang, Z.S., Zhu, R., Li, K.N., and Goldfarb, R.J. (2020) The giant Zaozigou orogenic Au-Sb deposit in West Qinling, China: Magmatic or metamorphic origin?. Mineralium Deposita , 55(2), 345–362.

Roda-Robles, E., Simmons, W., Pesquera, A., Gil-Crespo, P. P., Nizamoff, J., and Torres-Ruiz, J. (2015). Tourmaline as a petrogenetic monitor of the origin and evolution of the Berry-Havey pegmatite (Maine, USA). American Mineralogist, 100(1), 95-109.

Sillitoe, R.H. (2010) Porphyry copper systems. Economic Geology, 105(1), 3-41.

Slack, J.F., and Trumbull, R.B. (2011) Tourmaline as a recorder of ore-forming processes. Elements, 7(5), 321-326.

699 Smith, M.P., and Yardley, B.W.D. (1996) The boron isotopic composition of
700 tourmaline as a guide to fluid processes in the southwestern England
701 orefield: an ion microprobe study. Geochimica et Cosmochimica Acta, 60(8),
702 1415-1427.

703 Sui, J.X., Li, J.W., Jin, X.Y., Vasconcelos, P., and Zhu, R. (2018) $^{40}Ar/^{39}Ar$ and U-
704 Pb constraints on the age of the Zaozigou gold deposit, Xiahe-Hezuo
705 district, West Qinling orogen, China: relation to early Triassic reduced
706 intrusions emplaced during slab rollback. Ore Geology Reviews, 101, 885-
707 899.

708 Sun, W.D., Huang, R.F., Li, H., Hu, Y.B., Zhang, C.C., Sun, S.J., Zhang, L.P.,
709 Ding, X., Li, C.Y., Zartman, R.E. and Ling, M.X. (2015) Porphyry deposits
710 and oxidized magmas. Ore Geology Reviews, 65, 97-131.

711 Tonarini, S., Pennisi, M., Adorni-Braccesi, A., Dini, A., Ferrara, G., Gonfiantini,
712 R., Wiedenbeck, M., and Gröning, M. (2003) Intercomparison of boron
713 isotope and concentration measurements. Part I: selection, preparation and
714 homogeneity tests of the intercomparison materials. Geostandards
715 Newsletter, 27(1):21-39.

716 Trumbull, R.B., and Slack, J.F. (2018) Boron isotopes in the continental crust:
717 granites, pegmatites, felsic volcanic rocks, and related ore deposits. In Boron
718 Isotopes, 249-272. Springer, Cham.

van Hinsberg, V.J., Henry, D.J., and Dutrow, B.L. (2011) Tourmaline as a petrologic forensic mineral: A unique recorder of its geologic past. Elements, 7(5):327-332.

Wang, F. (2004) Genesis of Laodou Gold Deposit, Gansu Province, China. Gansu Metall, 02, 16-18 (in Chinese).

Williams-Jones, A. E., Bowell, R. J., and Migdisov, A. A. (2009). Gold in solution. Elements, 5(5), 281-287.

Yang, L.Q., Deng, J., Qiu, K.F., Ji, X.Z., Santosh, M., Song, K.R., Song, Y.H., Geng, J.Z., Zhang, C., and Hua, B. (2015a) Magma mixing and crust-mantle interaction in the Triassic monzogranites of Bikou Terrane, central China: Constraints from petrology, geochemistry, and zircon U-Pb-Hf isotopic systematics. Journal of Asian Earth Sciences, 98, 320-341.

Yang, L.Q., Deng, J., Dilek, Y., Qiu, K.F., Ji, X.Z., Li, N., Taylor, R.D., and Yu, J.Y. (2015b) Structure, geochronology, and petrogenesis of the Late Triassic Puziba granitoid dikes in the Mianlue suture zone, Qinling Orogen, China. Geological Society of America Bulletin, 11/12, 1831-1854.

Yang, S.Y., Jiang, S.Y., and Palmer, M.R. (2015) Chemical and boron isotopic compositions of tourmaline from the Nyalam leucogranites, South Tibetan Himalaya: implication for their formation from B-rich melt to hydrothermal fluids. Chemical Geology, 419, 102-113

739 Yang, S.Y., Jiang, S.Y., Zhao, K.D., Jiang, Y.H., Ling, H.F., and Luo, L. (2012)
740 Geochronology, geochemistry and tectonic significance of two Early
741 Cretaceous A-type granites in the Gan-Hang Belt, Southeast China. Lithos,
742 150, 155-170.

743 Yardley, B.W. (2005) Metal concentrations in crustal fluids and their relationship
744 to ore formation. Economic Geology 100th Anniversary, Vol 613-632.

745 Yu, H.C., Guo, C.A., Qiu, K.F., McIntire, D., Jiang, G.P., Gou, Z.Y., Geng, J.Z.,
746 Pang, Y., Zhu, R., and Li, N.B. (2019) Geochronological and Geochemical
747 Constraints on the Formation of the Giant Zaozigou Au-Sb Deposit, West
748 Qinling, China. Minerals, 9, 37.

749 Yu, H.C., Qiu, K.F., Nassif, M.T., Geng, J.Z., Sai, S.X., Duo, D.W., Huang, Y.Q.,
750 and Wang, J. (2020a) Early orogenic gold mineralization event in the West
751 Qinling related to closure of the Paleo-Tethys Ocean-Constraints from the
752 Ludousou gold deposit, central China. Ore Geology Reviews, 117, 103217.

753 Yu, H.C., Qiu, K.F., Sai, S.X., McIntire, D.C., Pirajno, F., Duo, D.W., Miggins,
754 D.P., Wang, J., Jia, R.Y., and Wu, M.Q. (2020b) Paleo-Tethys Late Triassic
755 Orogenic Gold Mineralization Recorded by the Yidi'nan Gold Deposit,
756 West Qinling, China. Ore Geology Reviews, 116, 103211.

757 Zhang, G.W., Zhang, B.R., Yuan, X.C., and Xiao, Q.H. (2001) Qinling orogenic
758 belt and continental dynamics. Science Press, Beijing 1–855.

759

760 **Figure Captains**

761 Figure 1. (a) Simplified geological map of the West Qinling orogen in central
762 China. The inset shows the location of the study area (modified after Zhang et al.,
763 2001; Dong et al., 2016; Qiu et al., 2017). (b) Geological sketch map of the
764 Xiahe-Hezuo polymetallic district showing locations of granitoids hosting
765 tourmaline samples analyzed in this study and their spatial distribution of related
766 ore deposits (modified after Qiu and Deng, 2017; Gou et al., 2019; Qiu et al.,
767 2020).

768

769 Figure 2. Quartz-tourmaline vein at Damai. (a, b) One 4 cm-wide quartz-
770 tourmaline vein hosted in biotite granodiorite with 3 cm-wide silicification
771 selvedge on both sides. Tourmalines appear as radial aggregates. (c) Biotite
772 granodiorite contains quartz, plagioclase, biotite, and hornblende. (d, e)
773 Tourmaline coexisting with quartz and minor sericite, contains quartz inclusions,
774 and replaces plagioclase. It exhibits a homogeneous light green center and wide
775 brown rim with oscillatory zoning. Amp = amphibole, Bt = biotite, Pl =
776 plagioclase, Qz = quartz, Ser = sericite, Tur = tourmaline. Note the $\delta^{11}B$ values
777 and spots locations. CPL = cross-polarized transmitted light, PPL = plane-
778 polarized transmitted light.

779

780 Figure 3. Tourmaline in tuffaceous breccia body from Dewulu. (a) Fine-grained

781 tourmaline and quartz rim the fragments of tuffaceous breccia. (b) Matrix
782 comprises quartz, plagioclase, sericite, and disseminated tourmaline, cementing
783 the fragments of tuffaceous breccia and sickle quartz. (c) Anhedral tourmaline
784 grains from tourmaline-quartz rim exhibit moderate pleochroism with small cyan
785 center and thin brown rim. Note the $\delta^{11}B$ values and spots locations.

786

787 Figure 4. Quartz-tourmaline veins (a, b), massive tourmaline veins (c, d), and
788 disseminated tourmalines (e) from Dewulu. (f) Tourmaline coexisting with
789 sericite replacing plagioclase. (g, h) Tourmalines are characterized by moderate
790 pleochroism and well-developed color growth zoning with a light green core and
791 light green to brown rim. (i) Tourmaline shows sector zoned centers. (j, k, l) The
792 tourmaline coexists with pyrite, arsenopyrite, chalcopyrite, quartz, with minor
793 rutile, and sericite. Note the $\delta^{11}B$ values and spots locations. A significant negative
794 shift of $\delta^{11}B$ values between cores and rims was observed. See text for details. Apy
795 = arsenopyrite, Ccp = chalcopyrite, Py = pyrite, Rt = rutile. RL = reflected light.

796

797 Figure 5. Quartz-tourmaline-magnetite veins from Meiwu. (a-c) Several quartz-
798 tourmaline-magnetite veins crosscut mafic enclaves found in granodiorite. (d-f)
799 Tourmaline coexisting with quartz, sericite, and magnetite, and replacing
800 plagioclase. Mag = magnetite. Note the $\delta^{11}B$ values and spots locations.

801

802 Figure 6. (a) Ternary classification of the tourmalines after Hawthorne and Henry
803 (1999) based on the principal constituents at the X-site; (b) Al–Fe–Mg ternary
804 diagram after Henry and Guidotti (1985) with compositions of tourmaline.
805 Labelled fields are: (1) Li-rich granitoid pegmatite and aplites, (2) Li-poor
806 granitoids, pegmatites and aplites, (3) Fe^{3+}- rich quartz–tourmaline rocks (altered
807 granitoids), (4) metapellites and metapsammites with Al-saturating phases, (5)
808 metapellites and metapsammites lacking Al-saturating phases, (6) Fe^{3+}-rich
809 quartz–tourmaline rocks, calc-silicate rocks and metapelites, (7) low-Ca
810 metaultramafic rocks and Cr–V-rich metasedimentary rocks, and (8) meta-
811 carbonates and meta-pyroxenites.

812

813 Figure 7. Geochemical compositions of tourmalines expressed in terms of atomic
814 ratio and atoms per formula unit (a.p.f.u.) after Pal et al., 2010. (a) Mg/(Mg + Fe)
815 versus Na/(Na + Ca), (b) Mg/(Mg + Fe) versus Ca (a.p.f.u.), (c) Al (a.p.f.u.)
816 versus Fe (a.p.f.u.), (d) Mg (a.p.f.u.) versus Fe (a.p.f.u.), (e) Al (a.p.f.u.) versus Na
817 (a.p.f.u.). The arrows in Figure c-e depict the trend of the major compositions of
818 the tourmalines. Data of average whole-rock major element composition of the
819 Damai, Dewulu, and Meiwu granitoids are from Luo et al. (2015) and Jin et al.
820 (2017).

821

822 Figure 8. Histograms of $\delta^{11}B$ values of tourmalines from Damai, Dewulu, and

Meiwu, and compiled boron reservoirs from Marschall and Jiang, 2011; Trumbull and Slack, 2018. MORB = mid-ocean ridge basalt.

Figure 9. Rayleigh fractionation models for evolution of $\delta^{11}B$ values of the Dewulu hydrothermal fluid systems, showing $\delta^{11}B$ variations of tourmaline during degassing. The vapor–fluid fraction factor (α) is assumed to be 1.0017 at 250 °C and 1.0012 at 295 °C taken from Leeman et al. (1992). Temperature data of ore-forming fluids (250–295 °C) are from Wang (2004) and Jin (2013). The initial $\delta^{11}B$ value is -5 ‰ assumed from the average $\delta^{11}B$ values from tourmalines in tourmaline in the tuffaceous breccia body. The large $\delta^{11}B$ isotopic fractionation decreasing from cores to rims indicates a relative large fraction of degassing ($F<0.2$).

Supplementary Tables

Supplementary Table 1. Summary of tourmaline samples investigated in this study.

Supplementary Table 2. Major element composition of tourmaline samples from the Xiahe-Hezuo polymetallic district.

843 Supplementary Table 3. Boron isotope of tourmaline samples from the Xiahe-

844 Hezuo polymetallic district.

FIG. 1

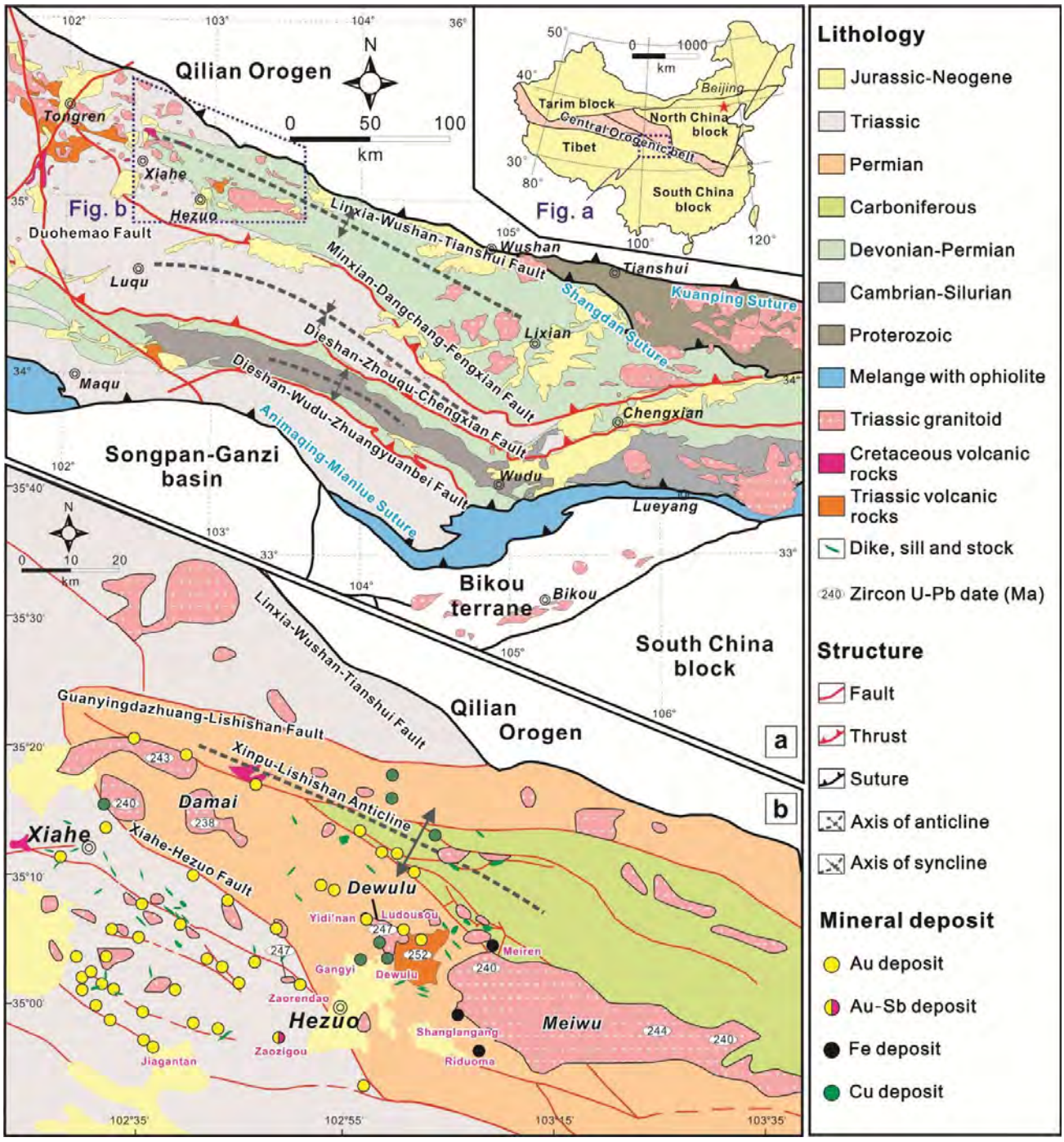
Qilian Orogen
Tongren
Xiahe
Hezuo
Fig. b
Duohemao Fault
Luqu
Linxia-Wushan-Tianshui Fault
Minxian-Dangchang-Fengxian Fault
Dieshan-Zhouqu-Chengxian Fault
Dieshan-Wudu-Zhuangyuanbei Fault
Animaqing-Mianlue Suture
Wushan
Tianshui
Lixian
Chengxian
Wudu
Maqu
Songpan-Ganzi basin
Shangdan Suture
Kuanping Suture
Lueyang
Bikou terrane
Bikou
South China block
Fig. a
Tarim block
North China block
Central Orogenic belt
Tibet
Beijing
Linxia-Wushan-Tianshui Fault
Qilian Orogen
Guanyingdazhuang-Lishishan Fault
Xinpu-Lishishan Anticline
Damai
Xiahe
Xiahe-Hezuo Fault
Dewulu
Yidi'nan
Ludousou
Meiren
Gangyi
Zaorendao
Hezuo
Zaozigou
Jiagantan
Shanglangang
Riduoma
Meiwu
a
b
Lithology
Jurassic-Neogene
Triassic
Permian
Carboniferous
Devonian-Permian
Cambrian-Silurian
Proterozoic
Melange with ophiolite
Triassic granitoid
Cretaceous volcanic rocks
Triassic volcanic rocks
Dike, sill and stock
Zircon U-Pb date (Ma)
Structure
Fault
Thrust
Suture
Axis of anticline
Axis of syncline
Mineral deposit
Au deposit
Au-Sb deposit
Fe deposit
Cu deposit

FIG. 2

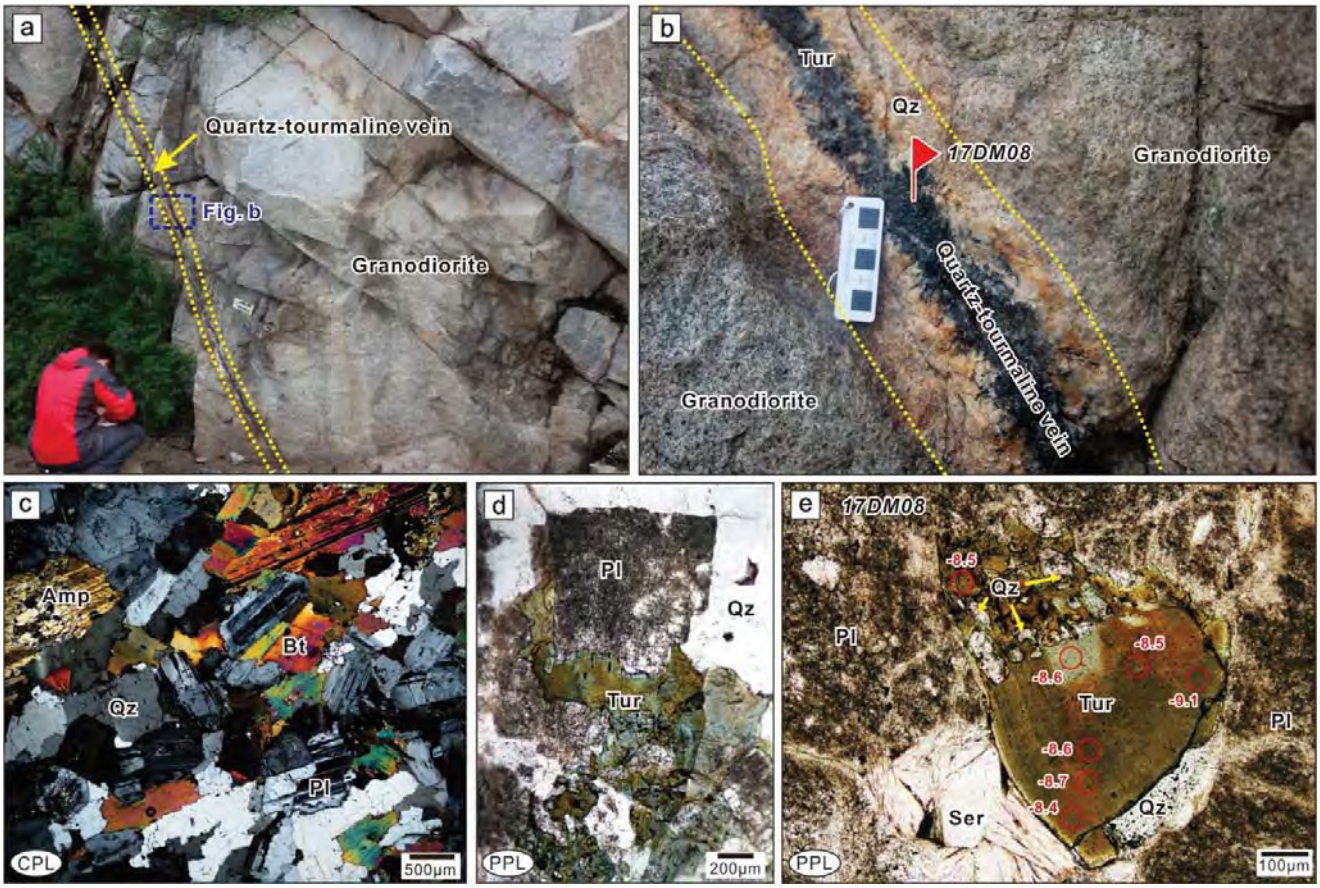
a
Quartz-tourmaline vein
Fig. b
Granodiorite
b
Tur
Qz
17DM08
Granodiorite
Quartz-tourmaline vein
Granodiorite
c
Amp
Bt
Qz
Pl
CPL
500μm
d
Pl
Qz
Tur
PPL
200μm
e
17DM08
-8.5
Qz
Pl
-8.5
-8.6
Tur
-9.1
Pl
-8.6
-8.7
-8.4
Ser
Qz
PPL
100μm

FIG. 3

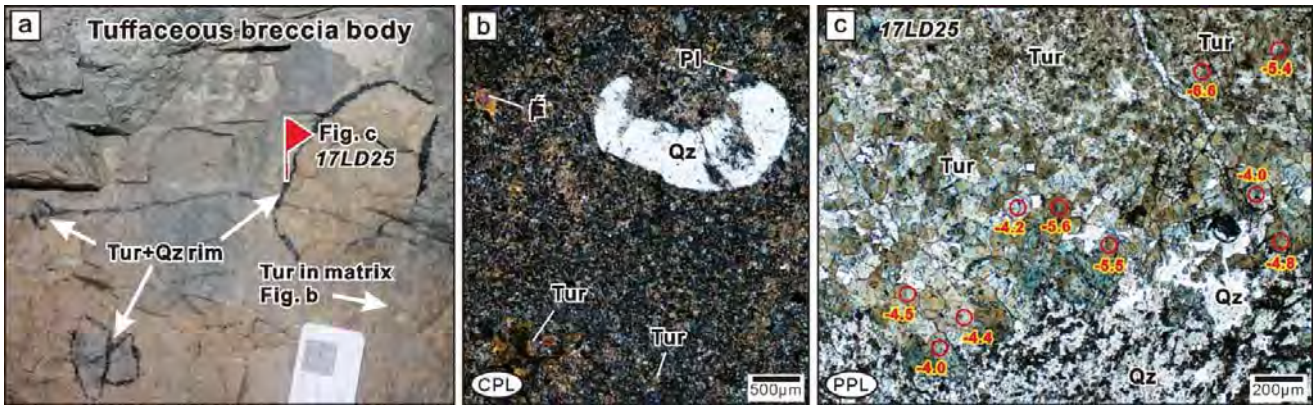
a
Tuffaceous breccia body
Fig. c
17LD25
Tur+Qz rim
Tur in matrix
Fig. b
b
Pl
Qz
Tur
Tur
CPL
500µm
c
17LD25
Tur
Tur
Tur
-5.4
-6.0
-4.0
-4.2
-5.6
-5.5
-4.8
-4.6
-4.4
-4.0
Qz
Qz
PPL
200µm

FIG. 4

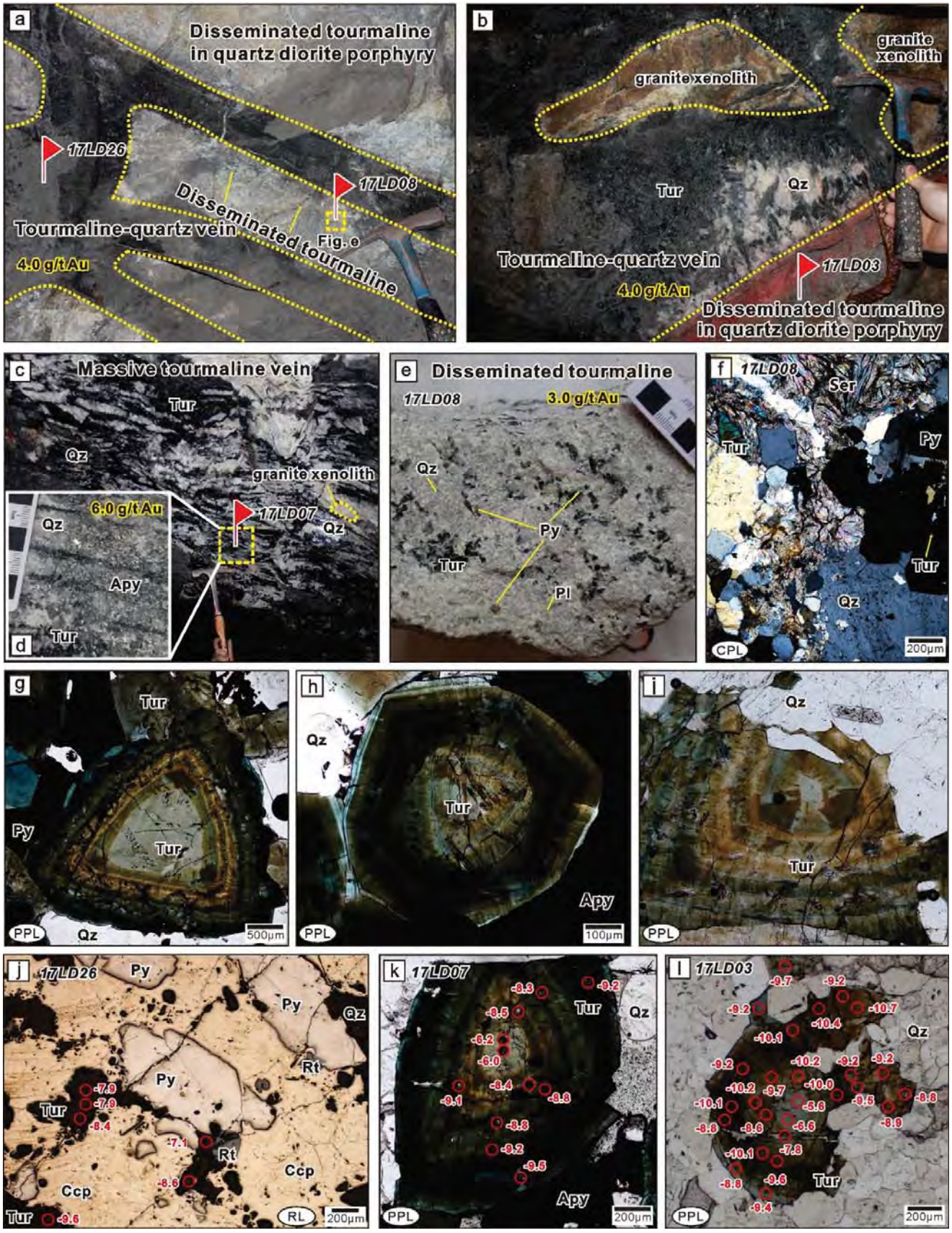
a
Disseminated tourmaline in quartz diorite porphyry
17LD26
17LD08
Disseminated tourmaline
Tourmaline-quartz vein
Fig. e
4.0 g/t Au
b
granite xenolith
granite xenolith
Tur
Qz
Tourmaline-quartz vein
4.0 g/t Au
17LD03
Disseminated tourmaline in quartz diorite porphyry
c
Massive tourmaline vein
Tur
Qz
granite xenolith
6.0 g/t Au
17LD07
Qz
Qz
Apy
d
Tur
e
Disseminated tourmaline
17LD08
3.0 g/t Au
Qz
Py
Tur
Pl
f
17LD08
Ser
Py
Tur
Tur
Qz
CPL
200μm
g
Tur
Py
Tur
PPL
Qz
500μm
h
Qz
Tur
Apy
PPL
100μm
i
Qz
Tur
PPL
j
17LD26
Py
Py
Qz
Rt
Py
-7.9
-7.9
Tur
-8.4
-7.1
Rt
Ccp
Ccp
-8.6
Tur
-9.6
RL
200μm
k
17LD07
-8.3
-9.2
-8.5
Tur
Qz
-6.2
-6.0
-8.4
-9.1
-8.8
-8.8
-9.2
-9.5
Apy
PPL
200μm
l
17LD03
-9.7
-9.2
-9.2
-10.7
-10.4
-10.1
Qz
-9.2
-10.2
-9.2
-9.2
-10.2
-9.7
-10.0
-10.1
-5.8
-9.5
-8.8
-8.8
-8.6
-6.6
-8.9
-10.1
-7.8
-8.8
-9.6
Tur
-8.4
PPL
200μm

FIG. 5

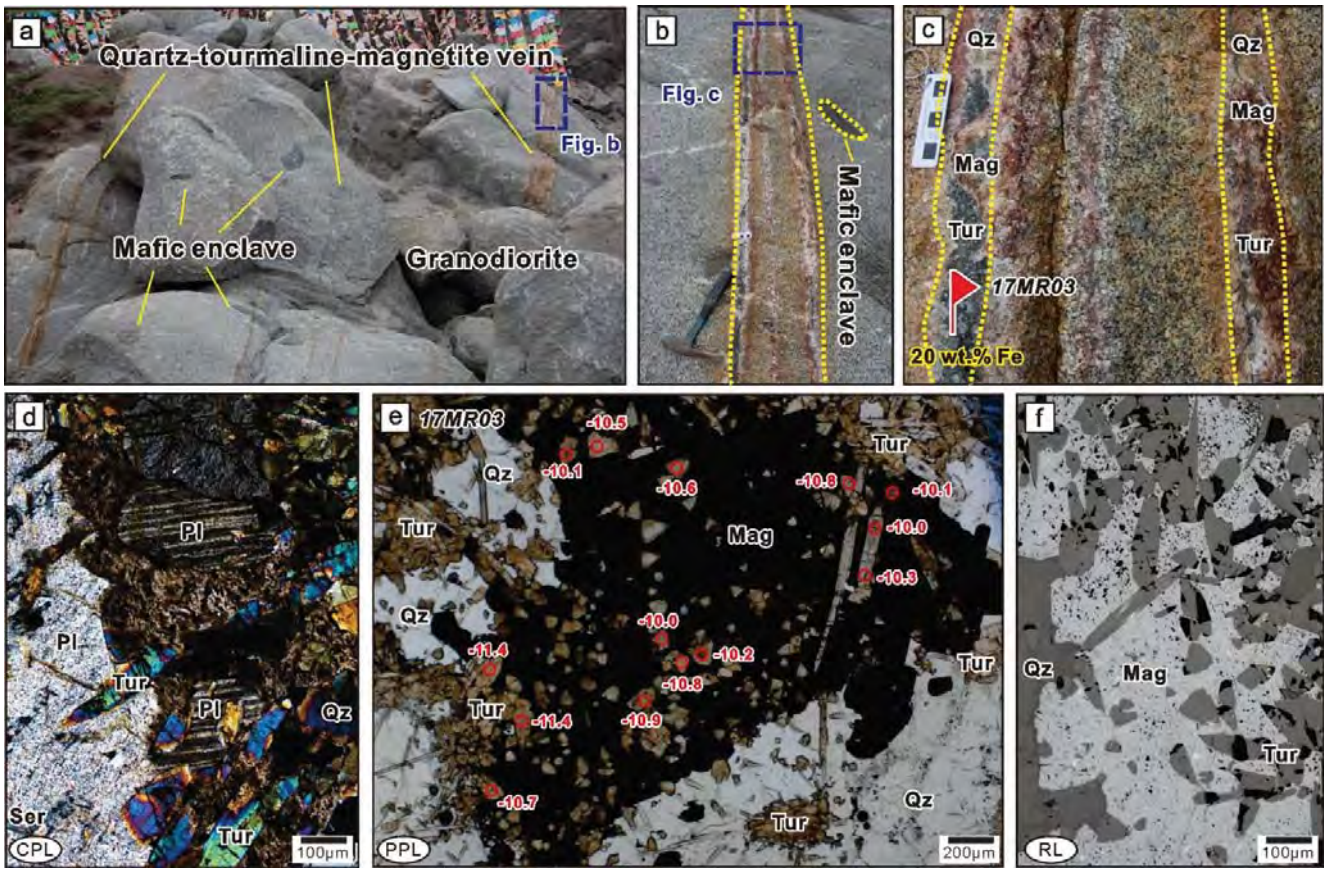
a
Quartz-tourmaline-magnetite vein
Fig. b
Mafic enclave
Granodiorite
b
Fig. c
Mafic enclave
c
Qz
Qz
Mag
Mag
Tur
Tur
17MR03
20 wt.% Fe
d
Pl
Pl
Tur
Pl
Qz
Ser
Tur
CPL
100μm
e
17MR03
-10.5
Tur
Qz
-10.1
-10.6
-10.8
-10.1
Tur
Mag
-10.0
-10.3
Qz
-10.0
-11.4
-10.2
Tur
-10.8
Tur
-11.4
-10.9
-10.7
Qz
Tur
PPL
200μm
f
Qz
Mag
Tur
RL
100μm

FIG. 6

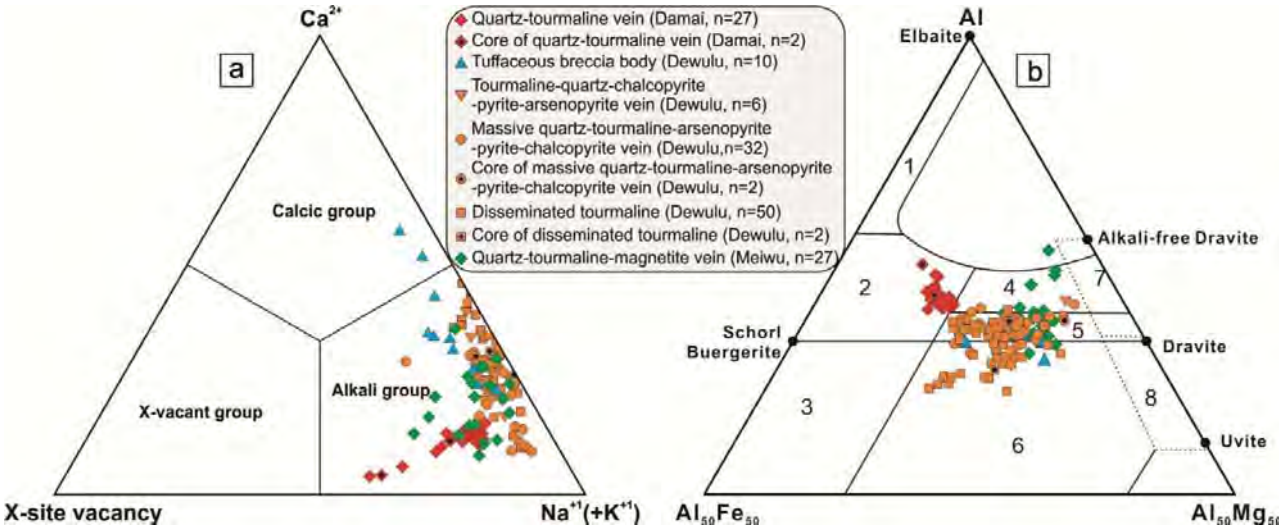
a
Ca2+
Calcic group
X-vacant group
Alkali group
X-site vacancy
Na+1(+K+1)
Quartz-tourmaline vein (Damai, n=27)
Core of quartz-tourmaline vein (Damai, n=2)
Tuffaceous breccia body (Dewulu, n=10)
Tourmaline-quartz-chalcopyrite -pyrite-arsenopyrite vein (Dewulu, n=6)
Massive quartz-tourmaline-arsenopyrite -pyrite-chalcopyrite vein (Dewulu,n=32)
Core of massive quartz-tourmaline-arsenopyrite -pyrite-chalcopyrite vein (Dewulu, n=2)
Disseminated tourmaline (Dewulu, n=50)
Core of disseminated tourmaline (Dewulu, n=2)
Quartz-tourmaline-magnetite vein (Meiwu, n=27)
b
Al
Elbaite
Alkali-free Dravite
Schorl
Buergerite
Dravite
Uvite
1
2
3
4
5
6
7
8
Al50Fe50
Al50Mg50

FIG. 7

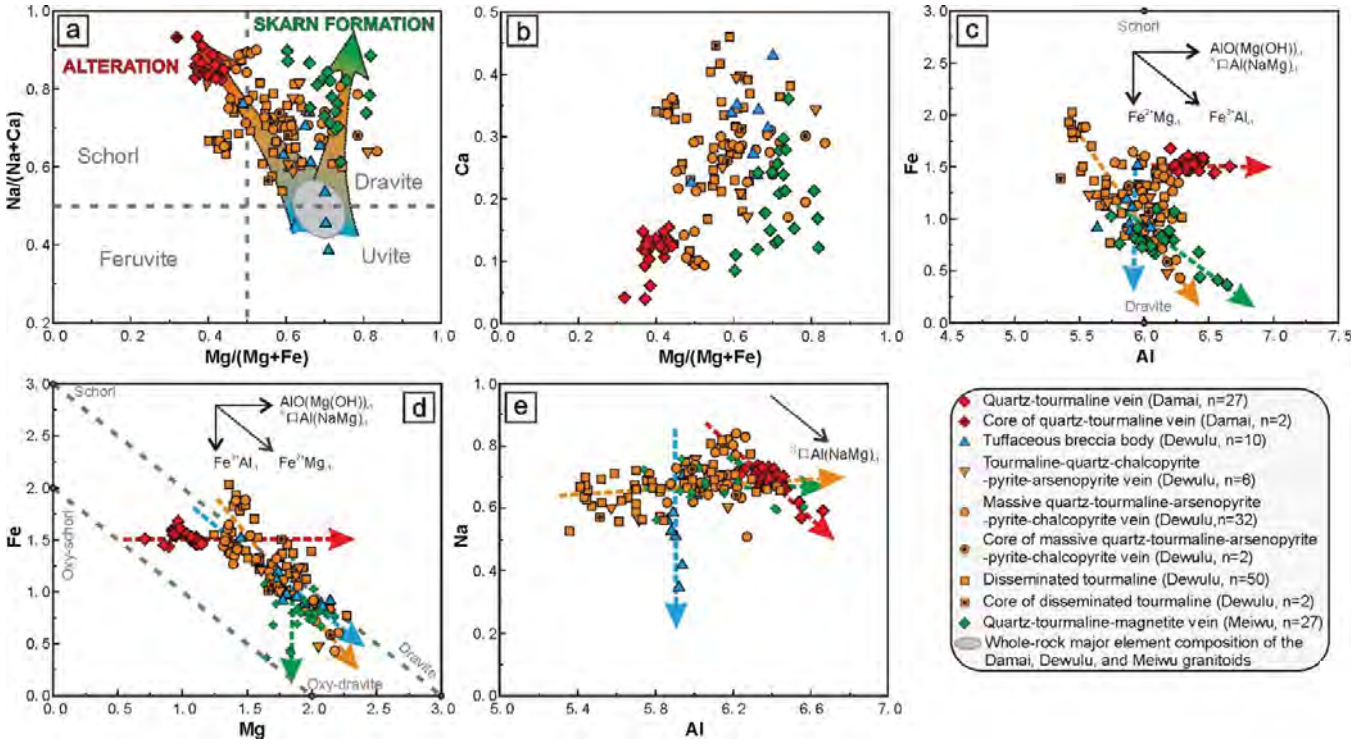
a
SKARN FORMATION
ALTERATION
Schorl
Dravite
Feruvite
Uvite
Na/(Na+Ca)
Mg/(Mg+Fe)
b
Ca
Mg/(Mg+Fe)
c
Schorl
AlO(Mg(OH))1
□Al(NaMg)1
Fe2+Mg-1
Fe3+Al-1
Dravite
Fe
Al
d
Schorl
AlO(Mg(OH))1
□Al(NaMg)1
Fe3+Al-1
Fe2+Mg-1
Oxy-schorl
Dravite
Oxy-dravite
Fe
Mg
e
□Al(NaMg)1
Na
Al
Quartz-tourmaline vein (Damai, n=27)
Core of quartz-tourmaline vein (Damai, n=2)
Tuffaceous breccia body (Dewulu, n=10)
Tourmaline-quartz-chalcopyrite -pyrite-arsenopyrite vein (Dewulu, n=6)
Massive quartz-tourmaline-arsenopyrite -pyrite-chalcopyrite vein (Dewulu,n=32)
Core of massive quartz-tourmaline-arsenopyrite -pyrite-chalcopyrite vein (Dewulu, n=2)
Disseminated tourmaline (Dewulu, n=50)
Core of disseminated tourmaline (Dewulu, n=2)
Quartz-tourmaline-magnetite vein (Meiwu, n=27)
Whole-rock major element composition of the Damai, Dewulu, and Meiwu granitoids

FIG. 8

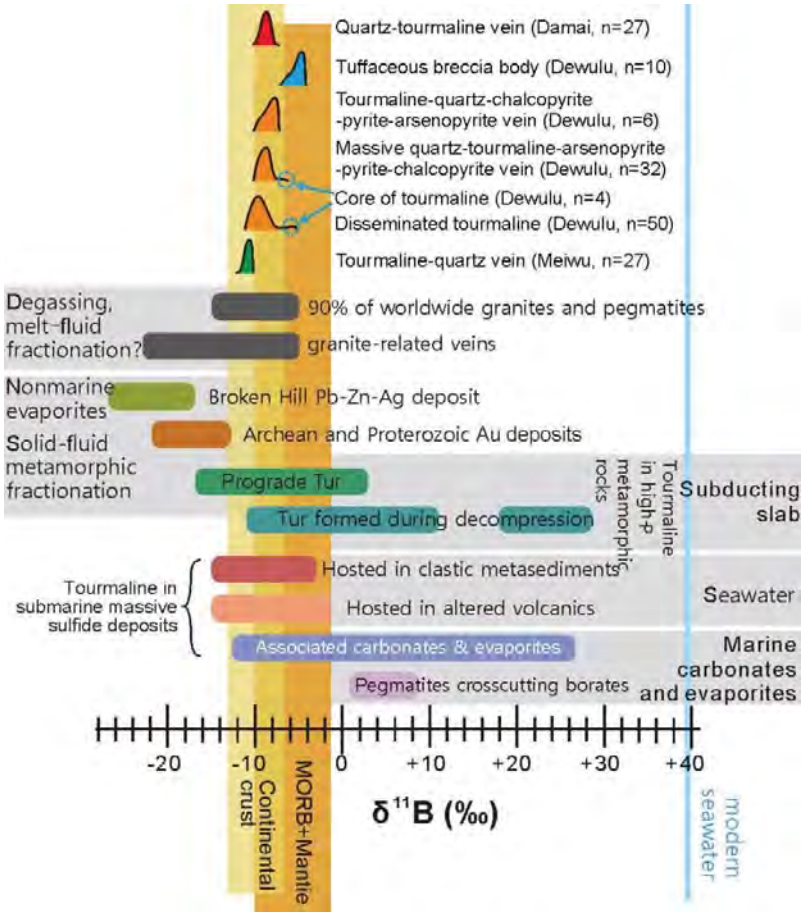
Quartz-tourmaline vein (Damai, n=27)
Tuffaceous breccia body (Dewulu, n=10)
Tourmaline-quartz-chalcopyrite -pyrite-arsenopyrite vein (Dewulu, n=6)
Massive quartz-tourmaline-arsenopyrite -pyrite-chalcopyrite vein (Dewulu, n=32)
Core of tourmaline (Dewulu, n=4)
Disseminated tourmaline (Dewulu, n=50)
Tourmaline-quartz vein (Meiwu, n=27)
Degassing, melt–fluid fractionation?
90% of worldwide granites and pegmatites
granite-related veins
Nonmarine evaporites
Broken Hill Pb-Zn-Ag deposit
Archean and Proterozoic Au deposits
Solid-fluid metamorphic fractionation
Prograde Tur
Tur formed during decompression
Tourmaline in high-P metamorphic rocks
Subducting slab
Tourmaline in submarine massive sulfide deposits
Hosted in clastic metasediments
Hosted in altered volcanics
Seawater
Associated carbonates & evaporites
Pegmatites crosscutting borates
Marine carbonates and evaporites
-20
-10
0
+10
+20
+30
+40
Continental crust
MORB+Mantle
δ11B (‰)
modern seawater

FIG. 9

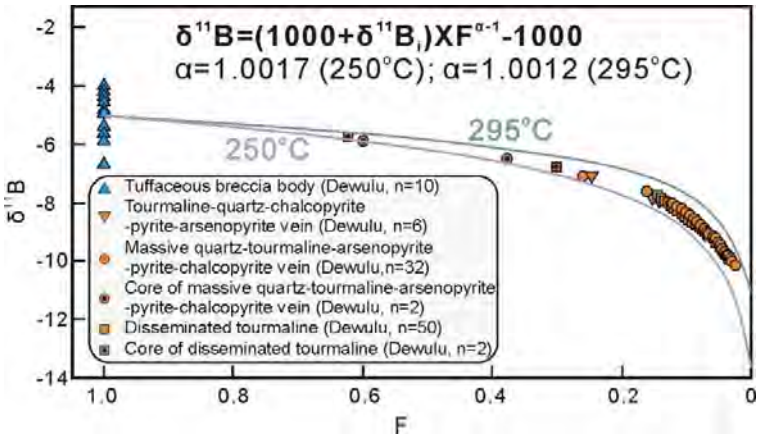
$\delta^{11}B=(1000+\delta^{11}B_i)XF^{\alpha-1}-1000$
α=1.0017 (250°C); α=1.0012 (295°C)
250°C
295°C
Tuffaceous breccia body (Dewulu, n=10)
Tourmaline-quartz-chalcopyrite -pyrite-arsenopyrite vein (Dewulu, n=6)
Massive quartz-tourmaline-arsenopyrite -pyrite-chalcopyrite vein (Dewulu,n=32)
Core of massive quartz-tourmaline-arsenopyrite -pyrite-chalcopyrite vein (Dewulu, n=2)
Disseminated tourmaline (Dewulu, n=50)
Core of disseminated tourmaline (Dewulu, n=2)
$\delta^{11}B$
-2
-4
-6
-8
-10
-12
-14
1.0
0.8
0.6
0.4
0.2
0
F